Towards the additive manufacturing of Zr-based metallic glasses using liquid phase sintering: Reactivity and phase transformation kinetics at the crystalline/amorphous interface

Maël Pontoreau, Olivier Dezellus, Sandrine Cardinal, Jean-marc Pelletier, Rodica Chiriac, Francois Toche, Philippe Steyer, Laurent Gremillard, Maxime Vallée, X Boulnat

Towards the Additive Manufacturing Of Zr-based Metallic Glasses Using Liquid Phase Sintering: reactivity and phase transformation kinetics at the crystalline/amorphous interface

Maël Pontoreau[a,c,*], Olivier Dezellus[b], Sandrine Cardinal[a], Jean-Marc Pelletier[a], Rodica Chiriac[b], François Toche[b], Philippe Steyer[a], Laurent Gremillard[a], Maxime Vallée[a], Xavier Boulnat[a]

[a] *INSA Lyon, CNRS, Université Claude Bernard Lyon 1, MATEIS, UMR 5510, F-69621 Villeurbanne, France.*
[b] *Université Claude Bernard Lyon 1, CNRS, LMI, UMR 5615, Lyon, France*
[c] *Univ. Bordeaux, CNRS, Bordeaux INP, ICMCB, UMR 5026, F-33600 Pessac, France*

Abstract

Bulk metallic glasses (BMG) present great potential for high-tech applications considering the excellent mechanical and corrosion properties. The on-going development of powder additive manufacturing techniques offers the opportunity to produce rather large parts composed of BMG. Relative to the sinter based additive manufacturing techniques, the sintering of a Zr-based BMG (AMZ4, $Zr_{59,3}Cu_{28,8}Al_{10,4}Nb_{1,5}$) using Zn-based additives was identified as promising: Zn alloys have indeed a melting point ($T_{m,Zn}$ = 419,5 °C) lower than the crystallization temperature of the BMG ($T_x \simeq$ 470 °C). Here, the study focuses on the understanding of the reactivity between AMZ4 and Zn as a function of temperature and time. A powder blend and a model interface AMZ4/Zn were studied combining *post-mortem* characterizations (SEM, EDX, XRD, micro-hardness...) with *in situ* characterization (DSC). Experimental construction of time-temperature-transformation diagram shows that there is a temperature/time window where sintering is permitted without crystallization. Beyond, an intermetallic phase is formed at the interface between the BMG and Zn, this phase was identified in terms of shape, composition and crystallography. A growth mechanism was proposed combining thermodynamic and kinetic aspects.

Keywords: metallic glasses, powder metallurgy, sintering, diffusion, thermal analysis, scanning electron microscopy

1. Introduction

Bulk metallic glasses (BMG) present attractive mechanical properties and corrosion resistance due to the absence of structural defects, such as dislocations and grain boundaries, usually found in crystalline materials. Since their recent discovery [1], more and more studies focus on their characterization, their synthesis or their

*Corresponding author.
Email address: mael.pontoreau@icmcb.cnrs.fr (Maël Pontoreau)

shaping due to their potential applications in many advanced fields (medical, aeronautics, ...). Nevertheless, there is a significant limitation on dimensions of BMG materials considering the manufacturing methods that can reach the critical cooling rate required to retain their amorphous structure.

In that framework, additive manufacturing (AM) techniques applied to BMG attracted much attention in the recent years. It would enable to overcome this dimensional limitation and to build complex shapes with minimal feedstock, *e.g.* powder, without inducing the crystallization of BMG. The production of microscopic metallic glass powder by gas atomization has been repeatedly reported in the literature with emphasis on morphology, size distribution, oxygen content and thermal stability. [2–4]. Due to their high glass-forming ability, numerous Zr-based metallic glass powders are even commercially available such as the industrial-grade alloy AMZ4 ($Zr_{59.3}Cu_{28.8}Al_{10.4}Nb_{1.5}$) with a particle size distribution suitable for AM techniques. To this day, it is also the most used and studied Zr-based BMG relative to AM [5]. So far, most studies focused on laser-based AM since the cooling rate is theoretically high enough to bypass crystallization and, therefore, to process BMG [6–10]. However, depending on the glass-forming ability of the initial powder and on the processing parameters, partial crystallization of BMG happens in the lower layers known as heat affected zones (HAZ) [10]. On the contrary, very few studies were devoted to the sinter-based AM (SBAM) techniques (direct ink writing, binder jetting, fused deposition modeling, metal injection moulding, etc.) [5]. Even if densification of metallic glass powders was reported using mostly spark plasma sintering (SPS) [11–14], it is still challenging to sinter BMG particles without mechanical pressure in order to retain the 3D printed shape.

Aiming at SBAM techniques, the liquid phase sintering of a metallic glass powder using metal-based additives was identified as promising. For example, Zn alloys could be used as biocompatible additives due to their melting temperature ($T_{m,Zn}$ = 419,5 °C) lower than the crystallization temperature of many BMG such as some Zr-based BMG ($T_x \simeq$ 470 °C for the industrial grade Zr-based metallic glass powder called AMZ4). Zn alloys would permit the densification of metallic glass powder compact via liquid phase sintering. For now, many challenges remain in understanding the interactions between the BMG and crystalline metals, whether solid or liquid.

In the literature, such interactions have been reported by few diffusion bonding studies [15–21]. Interestingly, Zhang et al. studied the joining process between a Zr-based BMG ($Zr_{62}Cu_{33}Al_4Ti$) and a Zn alloy (3 wt% Al) around 415°C, *i.e* above both the glass transition temperature of the BMG (T_g=410°C) and the liquidus temperature of the Zn alloy (T_L=397°C) [15, 16]. Using an ultrasound-assisted brazing method, joints with satisfactory mechanical properties (shear strength) were obtained and the growth of a reactive layer up to 17 μm was discussed relative to cavitation effects and Al and Zn diffusion into the Zr-based BMG. Even if most studies accomplished diffusion bonding in the supercooled liquid region of the BMG (*i.e.* between T_g and T_x) [15–18], Saadati *et. al.* elaborated a micron-sized dissimilar joint, between a Cu-based BMG ($Cu_{50}Zr_{43}Al_7$) and pure aluminium, 10 °C below the T_g of the BMG in order

to preserve amorphous structure and initial geometry of the BMG [20, 21]. Saadati *et. al.* emphasized the role of oxygen in the formation of the diffusion layer by proposing a bonding mechanism which relies on the dissolution and precipitation of surface oxide layers induced by elemental inter-diffusion at the interface. In the current study, the bonding mechanism will be discussed regarding both the oxide layer and possible diffusion paths in BMG. Some other studies commented the reactivity between BMG and crystalline metals by analyzing the as-formed interphase between BMG and crystalline metals in BMG/metal composites [22–31]. For example, aiming at mechanical properties, interpenetration phase composites were elaborated by casting a Zr based glass forming liquid into 3D stainless steel [22] or SiC ceramic foam [23]. The increase of the tensile plasticity [22] or fracture strength [23] was attributed, in both cases, to the formation of a nm- to μm-thick interphase. Nevertheless, these studies only focused on the analysis of the as-formed interphase without considering its growth mechanism. More commonly, BMG/metal composites were manufactured by consolidation of mixed powder using SPS [25–29]. Dudina *et. al.* showed that, in the case of a composite composed of a Al matrix and Fe-based BMG particles reinforcements, the growth of an interfacial layer highly depends on the temperature : no micrometer-sized interphase was detected for composites sintered at 500°C for 3 min whereas 10-15 μm thick interphase was characterized for composites sintered at 570°C for 3 min. Unfortunately, the other reported studies investigated the sintering of BMG/metals composite without varying the duration and the temperature of the heat treatment. These studies chose to focus on other parameters such as the volume fraction [26, 29] or the powder size of BMG [28]. In that framework, it was considered extremely appropriate to carry out a study on the reactivity between a BMG and crystalline metal considering the effect of several key parameters such as time and temperature of the heat treatment.

The present work focuses on the characterization of the reactivity between a Zr-based metallic glass powder and Zn additive metal around the T_g of the BMG and around the T_m of Zn. The goal of this study is twofold : (i) investigate the possibility of liquid sintering or brazing a Zr-based BMG using Zn metal and (ii) describe the reactivity between these two materials. For the first time, the system Zr-based BMG / Zn is investigated through two forms: powders blends and interdiffusion couples. The reactivity between Zr-based BMG and Zn will be described in details and compared to the crystallization kinetics of the sole BMG.

2. Materials and methods

2.1. Materials

The Zr-based BMG used in this study is a commercial gas-atomized powder with a nominal composition (at%) of $Zr_{59.3}Cu_{28.8}Al_{10.4}Nb_{1.5}$ (former trade name AMZ4, Heraeus GmbH, Germany). The glass transition temperature (T_g) and the crystallization onset temperature (T_x) of this BMG are 415.8 °C and 474.1 °C respectively at a heating rate of 30 K/min using a DSC Sensys Evo (SETARAM®) as described hereafter

(see 2.2). The corresponding heat flow curve of AMZ4 powder is reported in Supplementary Materials (see Figure S1) alongside with the heat flow curve of the Zn powder used (see Figure S2). The AMZ4 powder (particle size distribution : d_{v10} = 11.4 μm, d_{v50} = 20.2 μm, d_{v90} = 36.7 μm) was mixed with the Zn powder (purity > 99,5%, $T_{m,Zn,measured}$= 417.6 °C, d_{v10} = 5.5 μm, d_{v50} = 12.2 μm, d_{v90} = 28.6 μm) using a 3D shaker mixer (Turbula®) for 30 min to obtain a powder blend composed of 70 vol% of AMZ4 and 30 vol% of Zn (AMZ4/Zn, 70/30v). For AMZ4 and Zn powders, the oxygen contents were measured using an EMGA 620 W analyser from Horiba Jobin Yvon company and were equal to 782 ppm and 3555 ppm by weight (μg/g), respectively.

2.2. Differential scanning calorimetry

In order to investigate *in situ* the isothermal kinetics either of the crystallization of AMZ4 or of the reaction between AMZ4 and Zn, Differential Scanning Calorimetry (DSC) measurements were performed using a DSC Sensys Evo (SETARAM®) equipped with 3D sensor under Ar flow (10 mL/min, Air Liquide Alphagaz 2) for temperatures ranging from 325 °C to 450 °C. For each measurement, around 80 mg of powder were poured into an opened alumina crucible, kept under flowing Ar for 30 min at 25 °C, then heated from ambient temperature at 30 K/min until the isothermal temperature is reached. The latter was maintained long enough for the different events to occur. For these experiments, the AMZ4 powder and the blend of powders AMZ4/Zn (70/30v) were used. The data were analyzed using SETARAM software (CALISTO) and Python (libraries : lmfit, numpy and pandas). For each heat flow curve, the baseline was fitted using a polynomial function of order 2 before being substracted to the signal. The following treatments are detailed later in the results section (see 3.1).

2.3. Heat treatments in salt bath to simulate isothermal sintering

As the control of the temperature is critical, heat treatments of mixed powders were carried out using salt bath. AMZ4/Zn (70/30v) powder blends were encapsulated in quartz tube (inner diameter 3 mm, outer diameter 5 mm) under primary vacuum ($<5.10^{-2}$ mbar after 3 argon purges). The quartz tubes were then immersed in salt bath for different times (1 - 30 min) at different temperatures (350 – 425 °C) before being quenched into a water bath. Finally, the powders were recovered from the tubes to be analysed by X-Ray diffraction (XRD, Bruker AXS D8 Advance Diffractometer, Cu Kα radiation, 19-90°) and by scanning electron microscopy (SEM, Tescan Vega3) equipped with an energy-dispersive X-ray spectroscopy (EDX) detector.

2.4. Study of Plane Interfaces using Diffusion bonding experiments

In order to study the interface between AMZ4 and Zn, diffusion bonding experiments were carried out. AMZ4 and Zn powders were firstly independently sintered using SPS under vacuum with a uniaxial pressure

of 64 MPa and with a heating rate of 100 K/min: at 420 °C for 2 min for AMZ4 and 370 °C for 20 min for Zn. The relative density of sintered AMZ4 and Zn pieces were measured equal to 98.1 ± 0.5 % to 98.4 ± 0.3 % respectively using Archimedes' principle. The surfaces were then polished down to #4000 SiC paper and ultrasonically cleaned in an acetone bath for 3 min. Then, the two plates of 5 mm square and 3 mm thick were brought into contact and wrapped carefully with graphite sheets to form the AMZ4/Zn solid state interdiffusion couple. Then, the interdiffusion couple was placed in the graphite die and heat treated at 375 °C and 400 °C for 5, 20 and 60 min in SPS (64 MPa, vacuum, heating rate 100 K/min). The samples were then embedded in epoxy resin, mirror polished (diamond suspension, 1 μm) and analysed by SEM-EDX. Following the SEM analysis, micro-hardness measurements (10 gf, 10 s) were also performed on the embedded and polished samples along the studied interfaces using Micromet 5104 (Buehler®). Each reported Vickers hardness value is the average of at least five consecutive measurements.

For a better understanding, the different complementary experimental approaches are summarized on the Figure 1.

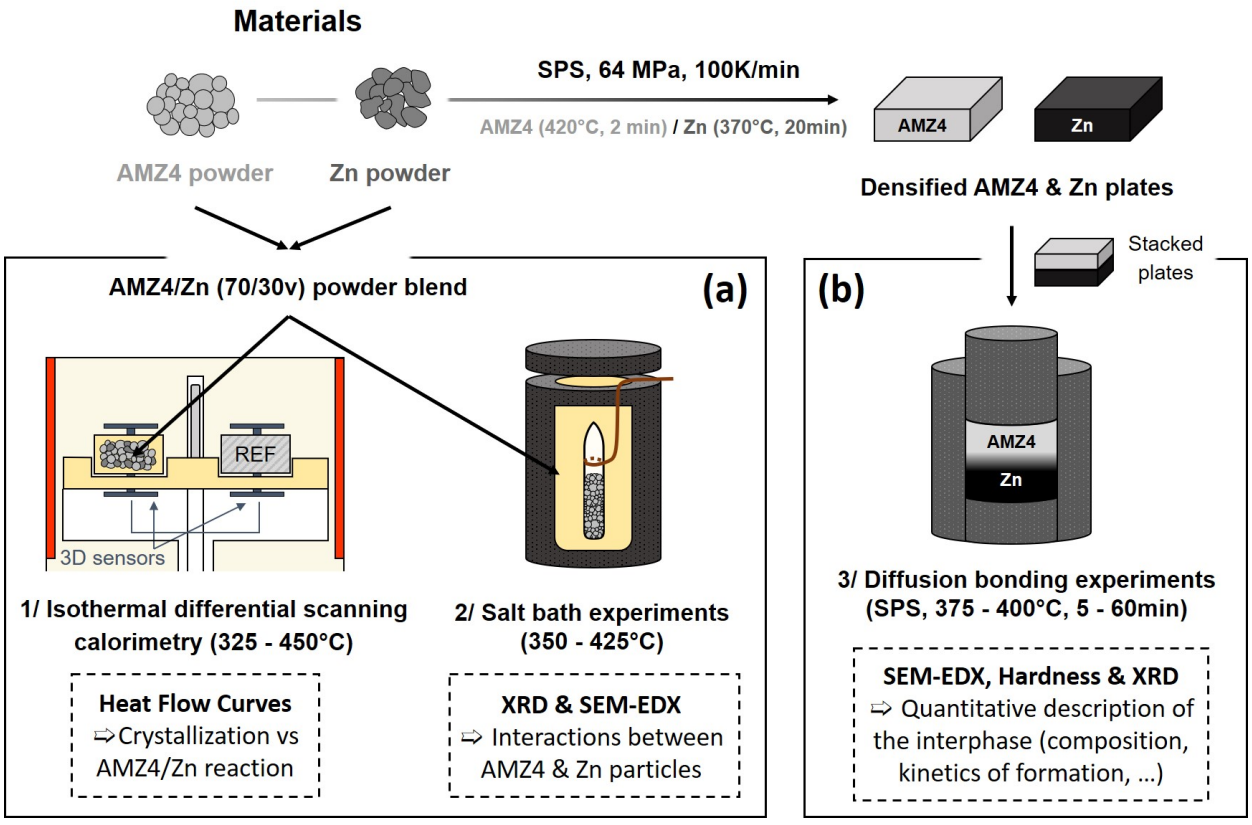

Figure 1: Representation of the experimental procedure for the study of the reactivity beetween AMZ4 and Zn powders : (a) experiments carried out on AMZ4/Zn (70/30v) powder blends and (b) diffusion bonding experiments of AMZ4/Zn interdiffusion couples

3. Results

3.1. Isothermal crystallization kinetics of AMZ4 and reaction kinetics of AMZ4/Zn system using DSC

Previous researchs investigated the isothermal crystallization kinetics of the industrial grade AMZ4 above its T_g using DSC measurements [8, 32]. Here, the isothermal crystallization kinetics of AMZ4 and reaction kinetics of AMZ4/Zn system are also studied below the T_g of AMZ4. Each heat flow curve (see Figure 2 a,c) displays a distinct exothermic peak whose temporality and shape change according to the temperature. In the case of AMZ4 powder, these peaks reflect the intrinsic crystallization of AMZ4 whereas, in the case of the AMZ4/Zn system, they highlight a reaction between AMZ4 and Zn. The use of the 3D sensor enables the detection of low intensity peaks for the AMZ4 powder after 200 min of holding time at 400°C, *i.e.* below the T_g of AMZ4, and for the AMZ4/Zn system after around 300 min of holding time at 325°C. For each sample, the first and second derivatives of the heat flow with regard to the time were calculated to identify the beginning (t_0) and the end (t_{endset}) of the exothermic peaks. After subtraction of the baseline, the progress of the reaction, X, as a function of time for a given isothermal temperature can be calculated using the heat flow associated with the event (dH/dt) via the equation 1 [32]. The Figure 2 (b,d) shows the computed evolutions of the reaction as a function of time (t=0 at the beginning of the holding step).

$$X(t)_T = \frac{\int_{t_0}^{t} (\frac{dH}{dt}) dt}{\int_{t_0}^{t_{endset}} (\frac{dH}{dt}) dt} \quad (1)$$

Firstly, concerning the kinetics of the intrinsic crystallization of AMZ4 and of the reaction between AMZ4 and Zn, the exothermic peaks were detected later and were more extended in time (logarithmic scale) when the temperature decreased. For example, the intrinsic crystallization of AMZ4 occured in less than 10 min at 450°C while it took more than 500 min at 400°C. Comparing the two systems, it is clear that the kinetics of the intrinsic crystallization and of AMZ4/Zn reaction are highly different: at 400 °C, the crystallization of AMZ4 began after 3 hours, whereas an intense exothermic peak was detected earlier than 10 min for the AMZ4/Zn powder blend. Moreover, the shape of the exothermic peaks are highly different which suggests that the intrinsic crystallization and the reaction between AMZ4 and Zn took place through very different mechanisms. The crystallization mechanism of BMG is complex and likely occurs in several steps starting with the growth of crystalline spherulites and ending with different crystalline phases [33–35]. The crystallization mechanism of AMZ4 will not be discussed hereafter as a dedicated study would be needed involving atomic-scale investigations (short-range order, nucleation of the nano crystallites, growth, etc) as shown by Gautier *et. al.* for a Ti-based BMG [33]. The mechanism linked to the AMZ4/Zn reaction will be discussed with direct observation later on.

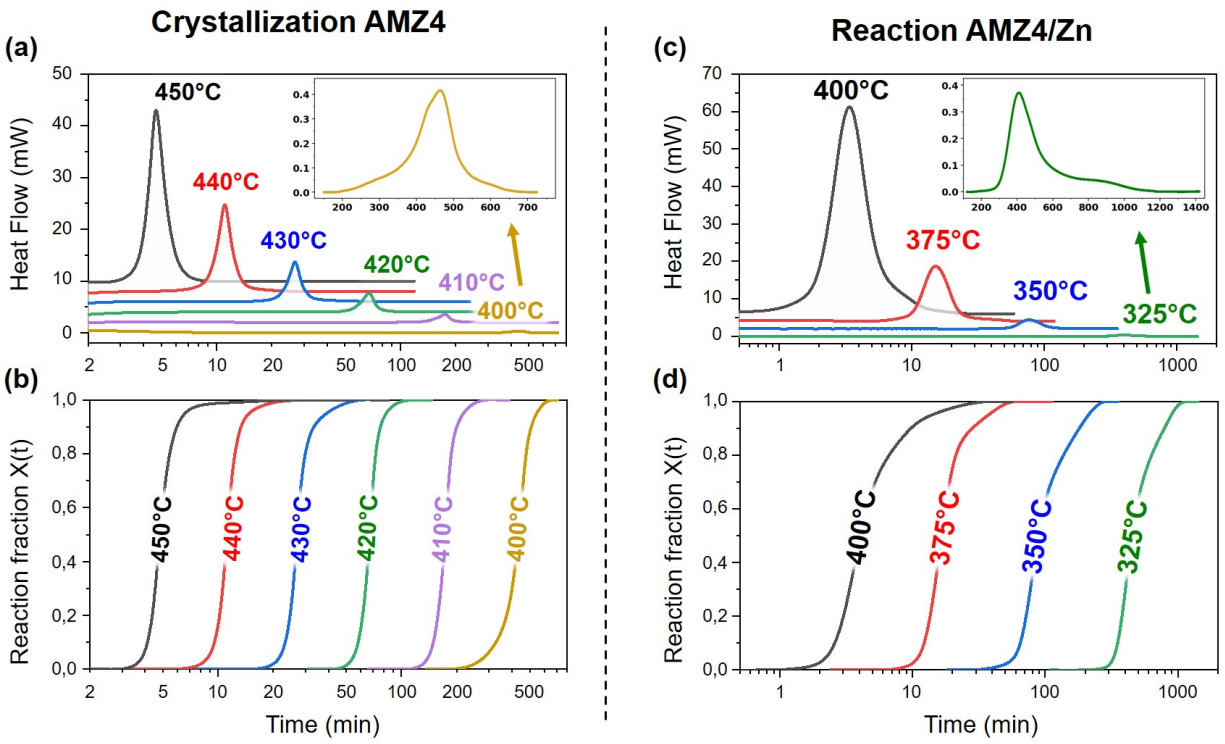

Figure 2: DSC results for AMZ4 (a,b) and AMZ4/Zn (70/30v) (c,d) samples: (a,c) Heat flow curves (325-450°C) measured by DSC, (b,d) reaction fraction as a function of time (log scale)

Based on these results, time-temperature-transformation (TTT) diagrams were constructed and are presented in Figure 3 (a). Similar TTT diagrams have already been determined upon heating and cooling for AMZ4 [8, 32]. The apparent activation energy of crystallization or of reaction (Ea) was also computed via an Arrhenius-like equation (Equation 2 [32]) as a function of the annealing time required to reach a certain reaction progress (t_X):

$$t_X = A * exp(\frac{E_a}{RT}) \tag{2}$$

with A a constant pre-exponential factor, T the temperature (in K) and R the universal gas constant. These plots show that the AMZ4/Zn reaction will always take place long before the intrinsic crystallization of AMZ4 (see Figure 3 (a)). This can be commented by analyzing the difference in activation energy of the reactions in the two systems (see Figure 3 (b)) : the activation energy is approx. 150 kJ/mol lower for the AMZ4/Zn reaction. If the values with the least uncertainty, *i.e.* between 30 and 60% of reaction progress, are averaged, the activation energy of crystallization of industrial grade AMZ4 powder and of the reaction between AMZ4 and Zn equals 365.5 ± 0.4 and 212.6 ± 1.3 kJ/mol respectively. The slight variations of the activation energy as a function of the reaction progress suggest that there is an evolution of the step that

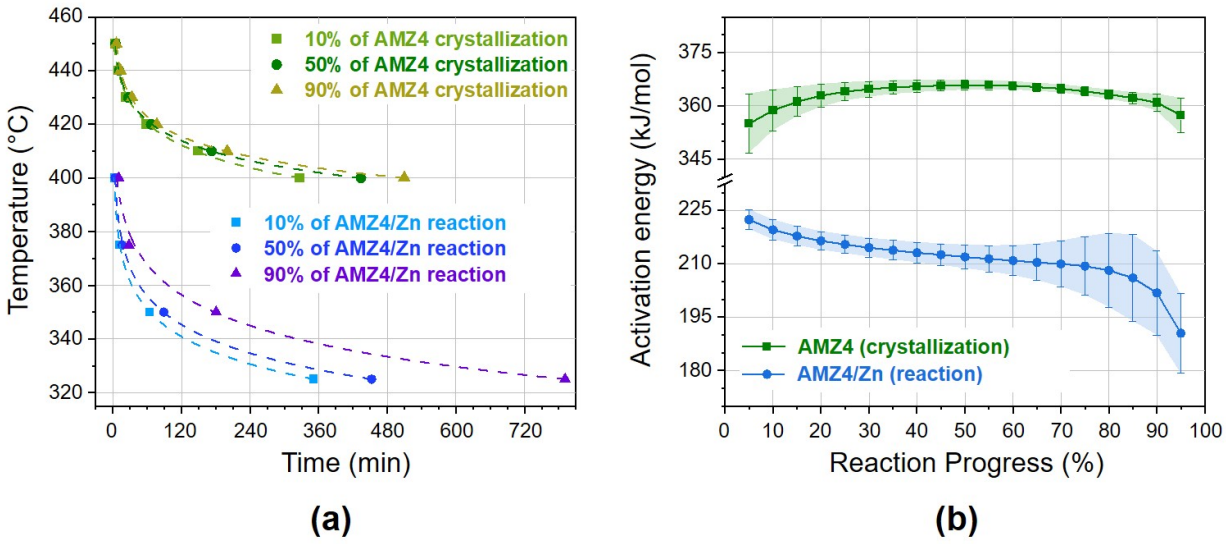

Figure 3: (a) Isothermal time-temperature-transformation (TTT) diagrams and (b) Activation energy as a function of reaction progress for both AMZ4 and AMZ4/Zn systems

controls the reaction over time. For example, different reactions can take place and the global reaction could start with an interfacial chemical reaction and continue with bulk diffusion. Once again, this will be more discussed later on (see 4.2). Concerning the liquid phase sintering of the system AMZ4/Zn, the kinetics of the reaction between Zn and AMZ4 powders seems too high below the melting point temperature of Zn ($T_{m,Zn}$ = 419,5 °C) to enable the liquid phase sintering of AMZ4. Even if it would be possible to avoid the crystallization of AMZ4 with a 20 min isothermal treatment at 425 °C, Zn particles would react with AMZ4 particles before melting. However, based on the TTT diagrams, heat treatments can be designed to control this reactivity, which could allow the consolidation of the AMZ4/Zn powder compact by solid state diffusion bonding.

3.2. Study of the AMZ4/Zn reaction using ex situ analysis

Post mortem analysis by XRD and SEM-EDX of powder blends immersed in salt bath for different times (1-30mn) at different temperature (350-425°C) enable to further investigate the reaction between AMZ4 and Zn particles. Experimentally, it was observed that, after all heat treatments, the powder compacts were still friable and were crushed using a spatula. This experimental observation indicated that the powder compacts did not densify enough to have a sufficient mechanical cohesion. Further characterizations were performed at a microscopic scale.

The Figure 4 shows XRD diffractograms for powder blends immersed in 400 °C salt bath for 5, 10 and 20 min and also a fully crystallized AMZ4 sample (reference). Initially, the powder blend is composed of Zn particles with defined diffraction peaks and amorphous AMZ4 particles which display a broad diffraction

peak between 2Θ=30° and 2Θ=50° characteristic of the amorphous phase. During the heat treatment at 400 °C, new crystalline peaks form at the expense of Zn peaks until no distinct Zn peaks can be detected after 20 min of heat treatment at 400 °C. These new peaks are only the result of the reaction between AMZ4 and Zn. Indeed, the new peaks do not correspond to the peaks that can be detected in a crystallized AMZ4 sample and the typical AMZ4 amorphous bump is still detected. Moreover, it can be considered that, for AMZ4/Zn (70/30v) powder blend, Zn is the limiting reactant and only a part of the amorphous volume of AMZ4 particles reacted with Zn particles. The newly formed crystalline phase(s) could not be identified using the common reference databases so that they will be referred as Reactive Affected Zone (RAZ) until its identification later in this article.

In order to estimate the respective evolution of the different phases, the integrated intensities of the peaks were used to compute the area fraction of each phase (AMZ4, Zn and RAZ phases) :

$$Area\ fraction\ of\ phase\ i = \frac{\sum Integrated\ intensity\ of\ phase\ i}{\sum Integrated\ intensity\ of\ all\ peaks} \tag{3}$$

The integrated intensity of the peaks has been determined by fitting each peak with pseudo-Voigt function using Lmfit Python Library [36]. As a function of time and temperature, 2D color maps with linear interpolation between experimental points were computed (see Figure 4 (b)). In comparison to the Figure 2, the kinetics determined by XRD is in accordance with the DSC curves and the TTT diagram, even if the experimental conditions are slightly different. For example, there is no heating ramp as the quartz tubes are directly immersed in the salt bath at the set temperature so that a slight incubation time must be taken into account. At 425°C, the formation of RAZ phase(s) is very fast : peaks relative to Zn phase are no longer detected after 5 min.

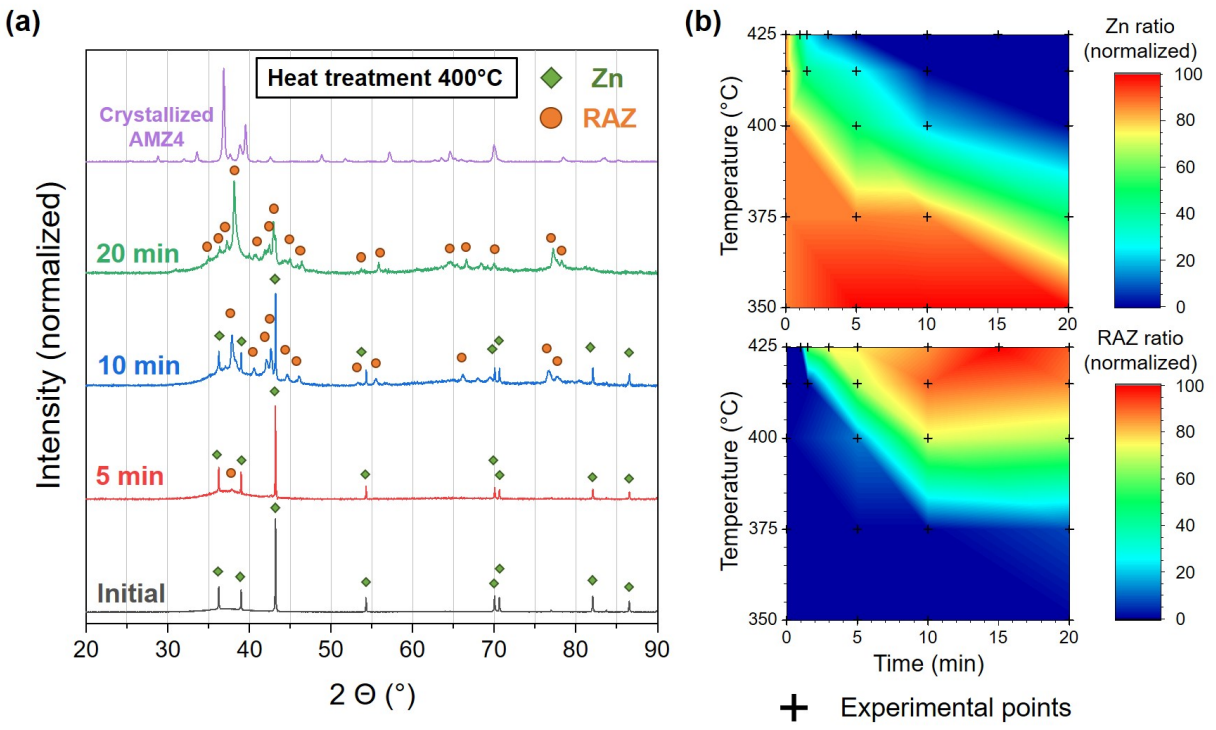

Figure 4: XRD diffractograms of salt bath experiments showing (a) diffractograms for heat treatment at 400°C and (b) 2D colour maps of the evolution of the fraction of Zn and RAZ phase(s) computed from integrated intensity of peaks as a function of time (0-20min) and temperature (350-425°C)

SEM-EDX analysis (see Figure 5) revealed that Zn particles reacted with AMZ4 particles by forming cones at the surface of AMZ4 particles rather than forming bridges between. This may explain the friability of the samples recovered from the tubes. Depending on the respective size of AMZ4 and Zn particles, the number and size of the cones varied from one particle to another during the heat treatment: for example, the smallest Zn particles reacted first with AMZ4 particles. SEM-EDX analysis of all heat treated samples suggests that the cones were likely formed by the solid state spreading of Zn on the surface of AMZ4 particles followed by interdiffusion and reaction between AMZ4 and Zn parts. Indeed, elemental distributions of the main elements showed that interdiffusion of the elements happened along the cones to the AMZ4 particles. Interestingly, the basis of the cones seems to be less concentrated in Cu than the top of the cone whereas the distribution of other elements is gradual from the basis to the top of the cone. Therefore, these different zones may reflect the presence of new crystalline phase(s) analyzed by XRD. The particular interdiffusion phenomena occurring during the reaction between Zn and AMZ4 particles must be studied in more detail using a model interface.

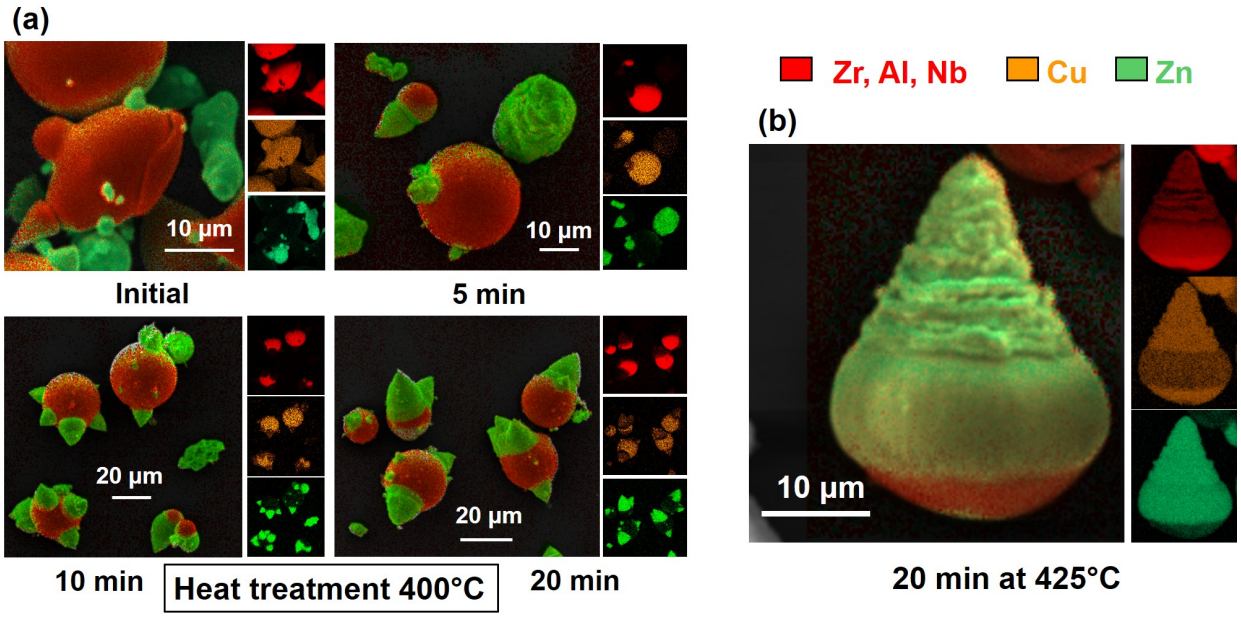

Figure 5: SEM-EDX analysis of salt bath experiments for AMZ4/Zn (70/30v) powder blends (a) for 0, 5, 10 and 20 min at 400°C and (b) 20 min at 425°C

3.3. Microstructural evolution of AMZ4/Zn interface

In order to facilitate the investigation of the reactivity between these two species, AMZ4/Zn model planar interfaces were synthesized and studied. In this way, the influence of the powder size distribution was not considered and quantitative EDX analysis were correctly performed. The Figure 6 presents the 110 μm thick interphase, the Zn/RAZ interface and the AMZ4/RAZ interface of the AMZ4/Zn interdiffusion couple heat treated at 400 °C for 60 min. One can notice that there are no unbounded regions, that the Zn/RAZ interface is much flatter than the AMZ4/RAZ interface and that micropores are present in the interphase close to the AMZ4/RAZ interface. Moreover, the chemical constrast suggests that there are two distinct zones composing the interphase close to the AMZ4/RAZ interface. The Figure 7 shows, for the 400 °C treated interdiffusion couples, the evolutions of the elemental distribution, measured via EDX line profiles, alongside the Vickers microhardness evolutions. Table 1 reports the measured lengths of the interphases for all interdiffusion couples using EDX analysis. The length of the interphase was measured using EDX line profiles (at least five line profiles per sample) and was defined as the length for which the atomic fraction of Zn goes from 100 at.% to 0 at.% and also for which the atomic fraction of Zr (resp. Cu) goes from 59.3 at.% (resp. 28.8%) to 0 at.%. As the AMZ4/RAZ interfaces are not perfectly flat, the uncertainty linked to the length of the interphase was increased to 2 μm.

In accordance with previous results, the growth of the interphase increases with time and, primarily, with temperature. At 400°C, the growth accelerates so drastically that the length of the interphase becomes

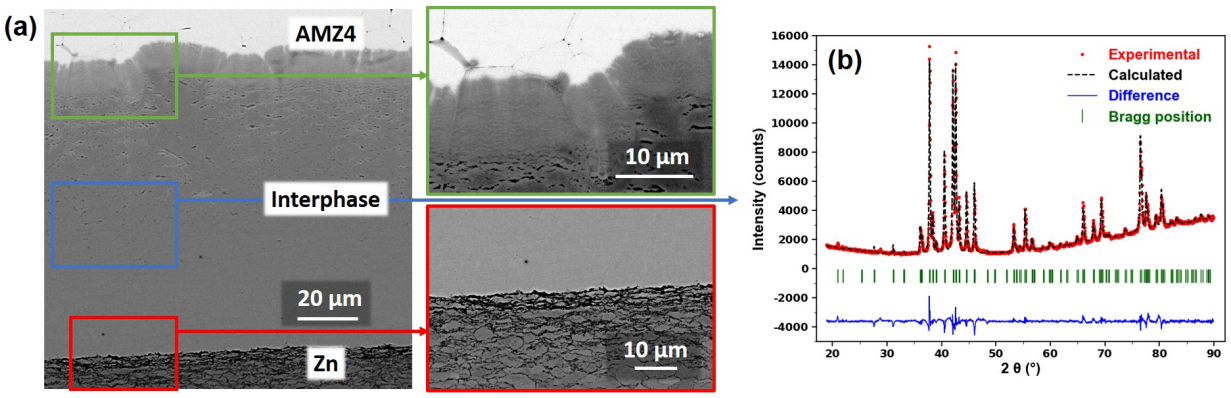

Figure 6: Analysis of AMZ4/Zn interdiffusion couple heat treated at 400°C for 60 min with (a) SEM analysis (Backscattered Electrons) of the interfacial region and (b) XRD analysis and Lebail refinement of the main interphase zone

Duration of heat treatment	**375°C**	400°C
5 min	Not bonded	18 ± 2 μm
20 min	13 ± 2 μm	83 ± 2 μm
60 min	45 ± 2 μm	110 ± 2 μm

Table 1: Length of the interphases for AMZ4/Zn interdiffusion couples measured by EDX

in approximately 5 min almost greater than the particle size of Zn and AMZ4 powders. On the contrary, the interdiffusion couple heat treated at 375°C for 5 min was not sufficiently bonded to carry out the analysis. For 20 min (resp. 60 min) of heat treatment, the length of the interphase is almost seven times (resp. three times) higher at 400°C than at 375°C. Even if the diffusion mechanism will be discussed later in this article (see 4.2), it can be highlighted that the growth of the interphase accelerates when the temperature approaches the supercooled liquid region of the BMG and the melting point temperature of Zn.

By analyzing the chemical compositions and mechanical properties of the interphase (see Figure 7), it is clear that the interphase is composed of two main distinct zones. First, there is a main zone which has a well defined composition (rich in Zn but with a small quantity of Zr, Cu, Al and O) and characterized by an intermediate hardness (270.4 ± 17.7 HV) between that of Zn (49.0 ± 1.1 HV) and that of AMZ4 (462.0 ± 31.8 HV). Its composition by EDX is: 91.5 ± 0.6 at.% Zn, 5.2 ± 0.5 at.% Zr and 3.3 ± 0.4 at.% Cu. A diffuse layer between this first zone and the Zn part can be noted where there is a slight segregation of Al and O atoms. This segregation can be explained taken into account the high stability of Al_2O_3 : Al atoms of AMZ4 would associate with O atoms initially present in the oxide layers of both AMZ4 and Zn. The location of the O atoms could be considered as a marker of the initial interface between AMZ4 and Zn. This would indicate that the interphase developed primarily by diffusion of Zn atoms into AMZ4 part. The length of this zone is systematically around 2 μm thick which is close to the uncertainties linked to EDX

measurements, that's why the composition of this narrow zone will not be discussed hereafter. The second zone is a wide transition zone where the quantity of Zr, Cu and Al (resp. Zn) increases (resp. decreases) drastically and where the measured hardness (around 600 HV) is higher that the hardness of the BMG. This high hardness value is due to the formation of some intermetallic compounds by elemental diffusion in this zone. In the case of the sample heat treated at 400°C for 5 minutes, the length of the second zone was too small compared to the size of the indentation to differentiate it from the first zone using the micro hardness measurements. This second zone may be composed of several phases and a whole study using Transmission electron microscopy (TEM) would be necessary. For this first study, taking into account the characterization techniques available, it has been chosen to focus on the evolution of the length of the two zones and on the characterization of the main first zone. Interestingly, the length of the main zone represents always around 70% of the total length of the interphase. Therefore, both zones grow together for the heat treatments studied : the first zone grows with a constant composition and the second zone also grows with a concentration gradient decreasing with time.

Finally, a last effort was made to try to determine the phase constituting the main part of the interphase. After a proper grounding of the sample heat treated at 400 °C for 60 min, this main zone was analysed by XRD (see Figure 6 (b)). Lebail refinement determined that the crystal structure of the major part of the interphase can be mostly described with the space group Fd-3m with a mesh parameter of 14.0777 10^{-10} m. Exploring crystal structure database computed using Density Functional Theory (DFT) and knowing its composition from EDX point measurements, it appears that the main zone shares many similarities with the DFT-calculated $Zr(Zn_{10}Cu)_2$ phase which exhibits a Fd-3m structure with a mesh parameter of 14.04 10^{-10} m (data retrieved from the Materials Project for $Zr(Zn_{10}Cu)_2$ (mp-1195710) from database version v2021.11.10). Certainly the chemical composition does not correspond exactly but it is close enough to suggest that the composition of the phase detected is indeed very close to this one.

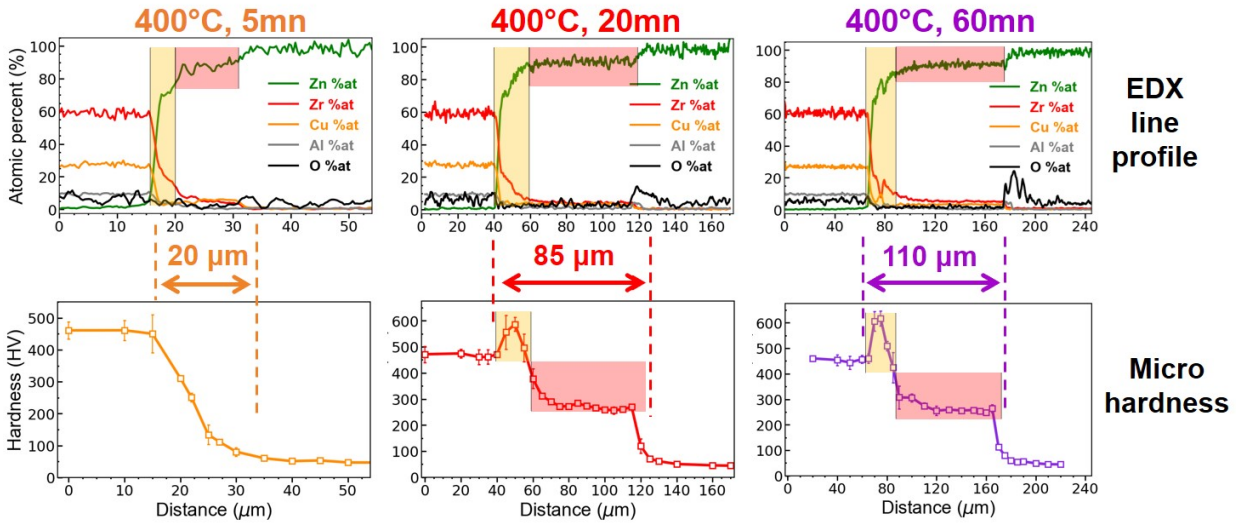

Figure 7: Evolution of elemental distribution (EDX) and hardness (micro hardness) along AMZ4/Zn interdiffusion couples heat treated at 400°C : the two main zones of the interphase are highlighted using yellow and red boxes

4. Discussion

4.1. On the reactivity for the powder mixtures relative to liquid sintering

The reactivity between AMZ4 and Zn was well established following three different experimental protocols. Even with slightly different experimental conditions, the salt bath experiments and the diffusion bonding experiments validated the TTT diagrams constructed from *in situ* DSC experiments. This diagram allows to understand which heat treatments AMZ4 can withstand without crystallizing and which heat treatments would initiate a reaction between AMZ4 and Zn. Even if there is a temperature/time window above $T_{m,Zn}$ where the sintering of AMZ4 would be permitted without intrinsic crystallization of the BMG, the reactivity is too high between AMZ4 and Zn below $T_{m,Zn}$ to allow the liquid phase sintering of AMZ4 (no grain rearrangement possible [37]). Moreover, the liquid phase sintering is all the less likely to occur as it seems that, during the reaction, the diffusion goes from Zn to AMZ4 particles. Indeed, for liquid phase sintering, it is commonly accepted that the solid phase must present high solubility in the additive (or liquid) phase but little reverse solubility (*i.e.* low solubility of the additive phase in the solid phase) [37]. In the case of the AMZ4/Zn (solid phase/additive phase) system, several experimental facts tend to say that the solubility of two species is the inverse of the ideal case. For AMZ4/Zn (70/30v) powder blends, Zn particles form cones at the surface of AMZ4 particles instead of bridges between particles. Then, for AMZ4/Zn interdiffusion couples, Zn/RAZ interface is perfectly flat whereas the RAZ/AMZ4 interface is wavy and it seems that the diffusion front progresses through a AMZ4 particle (see the green box in Figure 6). Moreover, as discussed earlier (see 3.3), the O atoms may be considered as markers of the initial oxide layers. The

location of these markers at the Zn/RAZ interface also indicates that Zn atoms mainly diffuse into AMZ4 and not the other way around. Subsequent studies could confirm this by introducing other markers at the interface before the heat treatment or by performing molecular dynamics simulations. Thereupon, it can be highlighted that a recent study, using molecular dynamics simulations, proves that the interdiffusion between pure Cu and amorphous $Cu_{50}Zr_{50}$ BMG is mainly attributed to the diffusion of Cu atoms into the amorphous structure [38]. More recently, Saadati *et. al.* also stated that, for a Cu-BMG/Al system, the growth of the reaction layer was mainly towards the BMG side rather than the pure metal side [21]. This could be explained regarding the high configurational entropy in the amorphous structure which prevents diffusion of elements outside the BMG. In any case, relative to liquid phase sintering, it is clear that the system AMZ4/Zn is not a proper candidate.

4.2. Thermodynamic aspects and diffusion mechanisms for interphase growth

Through *in situ* DSC experiments, the activation energy of the reaction between AMZ4 and Zn was estimated as equal to 212.6 ± 1.3 kJ/mol which was lower than the activation energy of the intrinsic crystallization of AMZ4 (365.5 ± 0.4 kJ/mol). Nevertheless, further comments can be made about the thermodynamic and kinetic aspects of the reaction between AMZ4 and Zn. Firstly, in the case of the AMZ4/Zn (70/30v) powder blends, it can be noted that the reactivity between AMZ4 and Zn is so high that the reaction can take place without the embrittlement of the oxide layer present on the surface of both Zn and AMZ4 particle's surfaces. This embrittlement could be achieved, for example, by the application of mechanical pressure or by the application of an electric current (cleaning effect known for SPS experiments). For BMG containing Zr, Cu and Al atoms, the oxide layer at the surface of as-received particles is composed of Al_2O_3, $CuAl_2O_4$ and/or ZrO_2 which are stable oxide phases [20]. However, the chemical affinitiy between Zn, Zr and Cu to form the $Zr(Zn_{10}Cu)_2$ phase would be high enough to promote the disruption of the oxide layer, that was not necessarily thick and continuous, leading to the formation of the interphase.

Dealing with the initial oxide layers, it has already been reported that the presence of oxygen accelerates the intrinsic crystallization of the BMG. Homogeneous nucleation of the oxygen-stabilized metastable phases would, then, act as heterogeneous nucleation sites for subsequent formation of the crystalline phases [4, 32, 39]. Therefore, oxygen atoms present at the initial AMZ4/Zn interface may play a role in the formation of the interphase. In this regard, it should be noted that Saadati *et. al.* proposed a diffusion bonding mechanism below the T_g, for their Cu-based BMG/Al system for which the diffusion of oxygen atoms plays a predominant role in the formation of 2 μm thick diffuse layers [21]. In the studied AMZ4/Zn system, oxygen concentrations measured by EDX in the two main zones composing the interphases (whose lengths are greater than 20 μm) is too low to explain the formation of all the interphase using the same mechanism. In other words, the mechanism proposed by Saadati *et. al.* could explain the very beginning of the growth of the interphase but, in this study, it was chosen to comment the further growth of a BMG/metal interphase.

In any case, the kinetics of the interphase formation highly depends on the time and temperature of the heat treatement as reported by the TTT diagram (see Figure 2) : the solid state mechanism involved is a largely temperature- and time-dependent process. As discussed in the previous paragraph (see 4.1), it seems that the diffusion process is dominated by the diffusion of Zn atoms into the amorphous structure. For now, it is still difficult to discuss about diffusion mechanisms concerning the BMG as they are unsteady and inhomogeneous materials for which there are no important elements commonly used in the crystal diffusion theory (such as grain boundaries, defects, lattice, etc.). It is generally accepted that, below the T_g, the diffusion coefficient of elements inside a BMG structure is low [20]. The formation of such a large interphase ($>100\mu$m for 60 min at 400°C) for this system below the T_g is therefore quite remarkable even considering a high thermodynamic driving force. Nevertheless, some defects exist in BMG which could explain the diffusion of Zn atoms inside AMZ4 part leading to the formation of a large interphase below the T_g. According to the "free volume" model, which is a popular approach when dealing defects in BMG [40, 41], regions of reduced density exist in BMG and act as vacancy-like defects. When approaching the T_g, more vacancy-like defects exist in the amorphous alloy [38] which would facilitate the diffusion of Zn atoms and the formation of the $Zr(Zn_{10}Cu)_2$ phase. According to the "free volume" model, the diffusion mode of Zn atoms inside AMZ4 would rely on a vacancy-like mechanism. Other approaches exist concerning the defect structure of BMG [40]. Then, it must be also considered that 400°C is not only close to the T_g of AMZ4 but also close to the T_m of Zn. Considering the interdiffusion couples heat treated at 400°C, the fact that the increase in length of the interphase slows down can be explained by the decrease of the concentration gradient in the second zone near the AMZ4/RAZ interface. To conclude, the formation and growth of the interphase would be explained (i) by a high chemical affinity between Zn, Zr and Cu leading to the formation of the $Zr(Zn_{10}Cu)_2$ phase, (ii) the increase with the temperature of both vacancy-like defects in the BMG and mobility of Zn atoms.

Finally, the Figure 8 represents in two dimensions a possible mechanism to explain the formation of the cones in the case of a powder blend. The cones would form due to a competition between diffusion of Zn on the surface of AMZ4 particles and the AMZ4/Zn reaction. First, the basis of the cones forms through the diffusion of Zn around AMZ4 particles. The mechanisms involved may be numerous such as surface diffusion or lattice diffusion from the surface. Interestingly, the vapor pressure of Zn exceeds 1 Pa from 340°C [42] which suggests that evaporation/condensation mechanism must also be involved. The relative significance of the different mechanisms involved will not be decided in this study. While the diffusion of Zn on the surface of AMZ4 particles occurs, the oxide layers at the interface AMZ4/Zn are disrupted due to the chemical affinity between Zn, Zr and Cu. Then, the reaction happens between Zn and AMZ4 particles through interdiffusion which initiates the formation of the RAZ. The interdiffusion then overrules the surface diffusion so that Zn particles stops spreading around AMZ4 particles which would fix the basis of the cones. The reaction between Zn and AMZ4 continues leading to the growth of the RAZ and to the formation of a

cone at the surface of the AMZ4 particles observed at the microscopic scale.

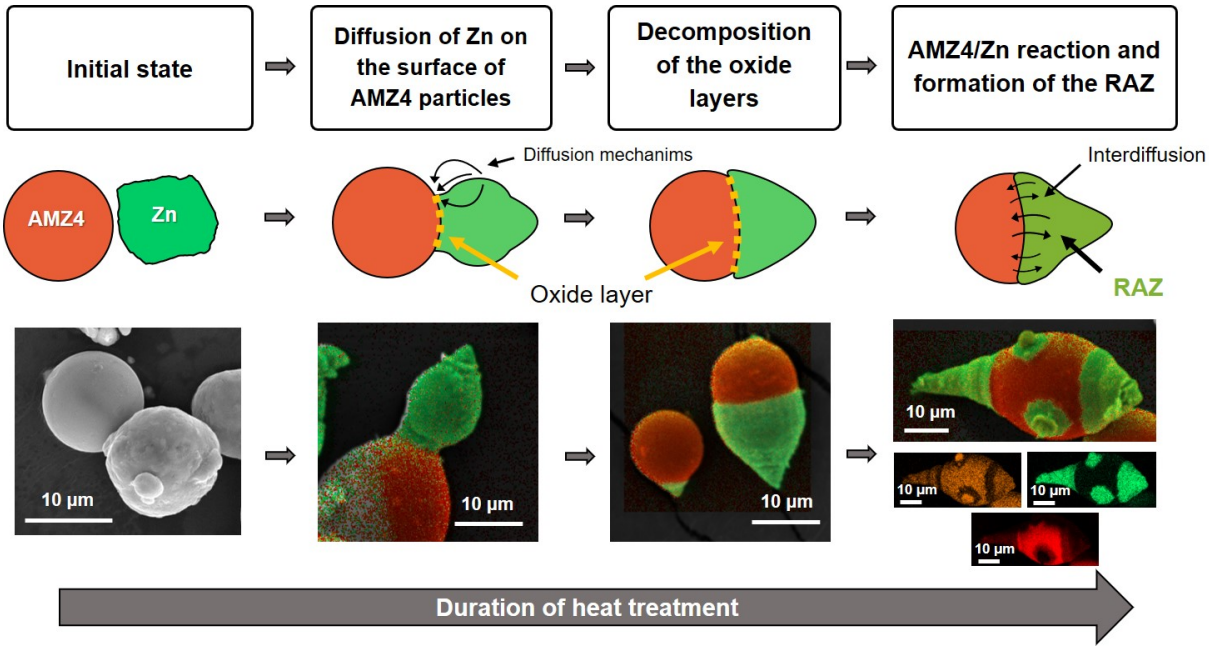

Figure 8: Dynamics of the reaction between Zn and AMZ4 particles leading to the formation of cones at the surface of AMZ4 particles : schematic representation and corresponding SEM micrographs

4.3. Possibilities for future works

Before starting the general conclusion, it is necessary to discuss the follow-up to be given to this work. Indeed, even if the use of Zn does not permit to perform the liquid phase sintering of the Zr-based BMG studied, several subjects of study can be developed from this work.

- First, it can be chosen to further study the AMZ4/Zn system in regard with diffusion bonding. Diffusion bonding of BMG is a great matter of interest in the field of metallic glass and the TTT diagram of the AMZ4/Zn can be used to optimize some AMZ4/Zn joints. Further study could also confirm the mechanisms associated with the formation of such an interphase.

- Then, still aiming at liquid phase sintering of AMZ4, future works could investigate other additive metals (resp. alloys) whose melting temperature (resp. liquidus or eutectic temperature) is lower than 400°C. For example, the use of a Zn alloy (5wt% Al) with an eutectic temperature around 380°C could be interesting. It would allow to determine to what extent the reaction depends on the T_g of AMZ4 or on the melting temperature (resp. liquidus or eutectic temperature) of the additive materials. With other additives containing no Zn atoms, the reaction between liquid additive and BMG particles could be limited enough to enable grain rearrangement and densification of the powder compacts.

- A final possibility would be to choose a BMG with higher T_g and crystallization temperature and to keep Zn as additive metals. The use of pure Zn as additive is interesting because of both its biocompatibility and its low melting point temperature.

As mentioned in the introduction, this kind of study is still lacking in the scientific literature, which is why they would be very valuable.

5. Conclusion

In this study, the reactivity between a Zr-based BMG and Zn pure metal was investigated using powder blends and interdiffusion couples. Effects of the temperature and the time of the heat treatment were highlighted by DSC, XRD, SEM-EDX and micro-hardness measurements. The determination of TTT diagrams by DSC measurements showed that there is a temperature/time window above $T_{m,Zn}$ where the sintering of AMZ4 would be permitted without intrinsic crystallization. Unfortunately, AMZ4 and Zn react with high kinetics below the T_g of AMZ4 (and so below $T_{m,Zn}$) forming a Reactive Affected Zone (RAZ). At 400 °C, the Zn phase vanishes completely in less than 10 min forming cones anchored in the AMZ4 particles rather than bridges between them.

The study of AMZ4/Zn interdiffusion couples enabled to analyze quantitatively the interdiffusion phenomena and the growth of RAZ as an interphase. The RAZ is composed of at least two zones: (i) a main zone close to the Zn/RAZ interface which has a define composition rich in Zn and (ii) a wide transition zone with concentration gradients. The crystal structure of the phase constituting the main zone corresponds to a Fd-3m structure (Lebail refinement) and is therefore close to the DFT-calculated $Zr(Zn_{10}Cu)_2$ phase (Fd-3m structure). The hardness of this phase equals 270.4 ± 17.7 HV. At the end, the formation of the RAZ was attributed to both a high chemical affinity between Zn, Zr and Cu associated with the formation of the $Zr(Zn_{10}Cu)_2$ phase and the increase with temperature of both vacancy-like defects in the BMG and mobility of Zn atoms.

To conclude, even if the liquid sintering of AMZ4 using Zn as additive phase is not possible, these experiments prove that the diffusion bonding between AMZ4 and Zn is possible and can be controlled. Consequently, Zn alloys could act as filler to join Zr-based BMG materials. These results are valuable, especially since the reaction takes place at temperatures below the T_g of the BMG (T_g = 409 °C) and would therefore allow the brazing of the BMG without risking its crystallization and the maintain of dimensional accuracy of the BMG.

Acknowledgments

This work was supported by LABEX MANUTECH-SISE (ANR-10-LABX-0075) of the Universite de Lyon, within the program "Investissements d'Avenir" (ANR-11-IDEX-0007) operated by the French National

Research Agency (ANR). The authors also thank Jérôme Andrieux for the XRD analysis (Lebail refinement).

Declaration of interest

Declarations of interest: none.

Data availability

The raw/processed data will be made available on request.

Bibliography

References

[1] W. Klement, R. H. Willens, P. Duwez, Non-crystalline structure in solidified gold-silicon alloys, Nature 187 (1960) 869–870. doi:https://doi.org/10.1038/187869b0.

[2] E. S. Barreto, M. Frey, J. Wegner, A. Jose, N. Neuber, R. Busch, S. Kleszczynski, L. Mädler, V. Uhlenwinkel, Properties of gas-atomized Cu-Ti-based metallic glass powders for additive manufacturing, Materials and Design 215 (2022) 110519. doi:10.1016/j.matdes.2022.110519.
URL https://doi.org/10.1016/j.matdes.2022.110519

[3] Y. F. Zhao, J. J. Si, J. G. Song, Q. Yang, X. D. Hui, Synthesis of Mg-Zn-Ca metallic glasses by gas-atomization and their excellent capability in degrading azo dyes, Materials Science and Engineering B: Solid-State Materials for Advanced Technology 181 (2014) 46–55. doi:10.1016/j.mseb.2013.11.019.

[4] W. Yan, Y. Liu, Y. Zhu, S. Niu, Glass-forming ability and thermal stability of gas- atomized $Zr_{50}Cu_{40}Al_{10}$ metallic glass powders, International Journal of Materials Research 102 (2011) 435–440.
URL https://doi.org/10.3139/146.110494

[5] N. Sohrabi, J. Jhabvala, R. E. Logé, Additive manufacturing of bulk metallic glasses—process, challenges and properties: A review, Metals 11 (2021). doi:10.3390/met11081279.

[6] Z. Chang, Y. Ge, L. Sun, W. Wang, J. Zhou, The micro-zones formation of Zr-based bulk metallic glass composite fabricated by laser 3D printing, Journal of Manufacturing Processes 76 (2022) 167–174. doi:10.1016/j.jmapro.2022.02.002.
URL https://doi.org/10.1016/j.jmapro.2022.02.002

[7] M. Frey, J. Wegner, N. Neuber, B. Reiplinger, B. Bochtler, B. Adam, L. Ruschel, S. S. Riegler, H. R. Jiang, S. Kleszczynski, G. Witt, R. Busch, Thermoplastic forming of additively manufactured Zr-based bulk metallic glass: A processing route for surface finishing of complex structures, Materials and Design 198 (2021) 109368. doi:10.1016/j.matdes.2020.109368.
URL https://doi.org/10.1016/j.matdes.2020.109368

[8] N. Sohrabi, J. Jhabvala, G. Kurtuldu, R. Frison, A. Parrilli, M. Stoica, A. Neels, J. F. Löffler, R. E. Logé, Additive manufacturing of a precious bulk metallic glass, Applied Materials Today 24 (2021) 101080. doi:10.1016/j.apmt.2021.101080.
URL https://doi.org/10.1016/j.apmt.2021.101080

[9] N. Sohrabi, J. Jhabvala, G. Kurtuldu, M. Stoica, A. Parrilli, S. Berns, E. Polatidis, S. V. Petegem, S. Hugon, A. Neels, J. F. Löffler, R. E. Logé, Characterization, mechanical properties and dimensional accuracy of a Zr-based bulk metallic glass manufactured via laser powder-bed fusion, Materials and Design 199 (2021). doi:10.1016/j.matdes.2020.109400.

[10] J. Wegner, M. Frey, M. Piechotta, N. Neuber, B. Adam, S. Platt, L. Ruschel, N. Schnell, S. Sebastian, H. ran Jiang, G. Witt, R. Busch, S. Kleszczynski, Materials and Design Influence of powder characteristics on the structural and the mechanical properties of additively manufactured Zr-based bulk metallic glass, Materials Design 209 (2021) 109976. doi:10.1016/j.matdes.2021.109976.
URL https://doi.org/10.1016/j.matdes.2021.109976

[11] Z. Wu, P. Du, T. Xiang, K. Li, G. Xie, Ti-based bulk metallic glass implantable biomaterial with adjustable porosity produced by a novel pressure regulation method in spark plasma sintering, Intermetallics 131 (2021) 107105. doi:10.1016/j.intermet.2021.107105.
URL https://doi.org/10.1016/j.intermet.2021.107105

[12] H. Ding, Z. Zhao, J. Jin, L. Deng, P. Gong, X. Wang, Densification mechanism of Zr-based bulk metallic glass prepared by two-step spark plasma sintering, Journal of Alloys and Compounds 850 (2021) 156724. doi:10.1016/j.jallcom.2020.156724.
URL https://doi.org/10.1016/j.jallcom.2020.156724

[13] P. Drescher, K. Witte, B. Yang, R. Steuer, O. Kessler, E. Burkel, C. Schick, H. Seitz, Composites of amorphous and nanocrystalline Zr–Cu–Al–Nb bulk materials synthesized by spark plasma sintering, Journal of Alloys and Compounds 667 (2016) 109–114. doi:10.1016/j.jallcom.2016.01.161.
URL http://dx.doi.org/10.1016/j.jallcom.2016.01.161

[14] S. Cardinal, J. M. Pelletier, J. C. Qiao, G. Bonnefont, G. Xie, Influence of spark plasma sintering parameters on the mechanical properties of $Cu_{50}Zr_{45}Al_5$ bulk metallic glass obtained using metallic glass powder, Materials Science and Engineering A 677 (2016) 116–124. doi:10.1016/j.msea.2016.09.032.
URL http://dx.doi.org/10.1016/j.msea.2016.09.032

[15] X. Zhang, D. Li, L. Wang, C. Wan, L. Song, K. Song, Y. Xiao, Ultrasonic brazing of Zr-based bulk metallic glass and 1060 Al alloy using Zn-3Al filler metal, Journal of Advanced Joining Processes 5 (2022) 100095. doi:10.1016/j.jajp.2022.100095.
URL https://doi.org/10.1016/j.jajp.2022.100095

[16] X. Zhang, Y. Xiao, L. Wang, C. Wan, Q. Wang, H. Sheng, M. Li, Ultrasound-induced liquid/solid interfacial reaction between Zn-3Al alloy and Zr-based bulk metallic glasses, Ultrasonics Sonochemistry 45 (2018) 86–94. doi:10.1016/j.ultsonch.2018.03.006.
URL https://doi.org/10.1016/j.ultsonch.2018.03.006

[17] K. Hongchao, G. Heng, W. Jun, T. Bin, L. Jinshan, Diffusion bonding between Zr-based metallic glass and copper, Rare Metal Materials and Engineering 45 (2016) 42–45. doi:10.1016/s1875-5372(16)30043-1.
URL http://dx.doi.org/10.1016/S1875-5372(16)30043-1

[18] C. Wen, T. Shi, B. Chen, Z. Zhu, Y. Peng, G. Liao, Diffusion bonding of $Zr_{55}Cu_{30}Ni_5Al_{10}$ bulk metallic glass to Cu with Al as transition layer, Materials and Design 83 (2015) 320–326. doi:10.1016/j.matdes.2015.06.028.
URL http://dx.doi.org/10.1016/j.matdes.2015.06.028

[19] Y. Zhu, G. Liao, T. Shi, Z. Tang, M. Li, Interdiffusion cross crystal-amorphous interface: An atomistic simulation, Acta Materialia 112 (2016) 378–389. doi:10.1016/j.actamat.2016.04.032.

[20] A. Saadati, M. Malekan, F. Khodabakhshi, Under glass transition temperature diffusion bonding of bulk metallic glass and aluminum, Materials Chemistry and Physics 269 (2021) 124758. doi:10.1016/j.matchemphys.2021.124758.
URL https://doi.org/10.1016/j.matchemphys.2021.124758

[21] A. Saadati, M. Malekan, F. Khodabakhshi, G. Wilde, A. P. Gerlich, Dissimilar diffusion bonding of bulk metallic glass: Amorphous/crystalline atomic-scale interaction, Materials Characterization (2022) 112480doi:10.1016/j.matchar.2022.112480.

[22] W. J. Gao, W. W. Zhang, T. Zhang, C. Yang, X. S. Huang, Z. Y. Liu, Z. Wang, W. H. Li, W. R. Li, L. Li, L. H. Liu, Large tensile plasticity in Zr-based metallic glass/stainless steel interpenetrating-phase composites prepared by high pressure die

casting, Composites Part B: Engineering 224 (2021). doi:10.1016/j.compositesb.2021.109226.

[23] X. Su, Z. Qi, H. Qu, J. Zhang, Y. Shen, Y. Cao, G. Chen, Effects of pore density on microstructure and mechanical properties of porous SiC ceramic foam/Zr-based metallic glass interpenetrating phase composites, Intermetallics 129 (2021) 106964. doi:10.1016/j.intermet.2020.106964.
URL https://doi.org/10.1016/j.intermet.2020.106964

[24] Z. Li, S. Wu, X. Huang, N. Li, Versatile fabrication of bulk metallic glass composites reinforced by dissimilar secondary phase, Materials Science and Engineering A 791 (2020). doi:10.1016/j.msea.2020.139643.
URL https://doi.org/10.1016/j.msea.2020.139643

[25] D. V. Dudina, B. B. Bokhonov, I. S. Batraev, Y. N. Amirastanov, A. V. Ukhina, I. D. Kuchumova, M. A. Legan, A. N. Novoselov, K. B. Gerasimov, I. A. Bataev, K. Georgarakis, G. Y. Koga, Y. Guo, W. J. Botta, A. M. Jorge, Interaction between $Fe_{66}Cr_{10}Nb_5B_{19}$ metallic glass and aluminum during spark plasma sintering, Materials Science and Engineering A 799 (2021). doi:10.1016/j.msea.2020.140165.

[26] L. Zhang, B. Li, H. Wu, W. Wang, S. Zhai, J. Xu, Z. Niu, Y. Wang, Microstructure and property characterization of Al-based composites reinforced with CuZrAl particles fabricated by mechanical alloying and spark plasma sintering, Advanced Powder Technology 29 (2018) 1695–1702. doi:10.1016/j.apt.2018.04.004.
URL https://doi.org/10.1016/j.apt.2018.04.004

[27] Z. Wang, K. Georgarakis, K. S. Nakayama, Y. Li, A. A. Tsarkov, G. Xie, D. Dudina, D. V. Louzguine-Luzgin, A. R. Yavari, Microstructure and mechanical behavior of metallic glass fiber-reinforced Al alloy matrix composites, Scientific Reports 6 (2016) 1–11. doi:10.1038/srep24384.
URL www.nature.com/scientificreports

[28] G. Xie, Z. Huang, Optimizing mechanical and electrical properties of Cu-coated Cu–Zr–Al bulk metallic glass composites by adjusting glassy powder size, Intermetallics 146 (2022). doi:10.1016/j.intermet.2022.107570.

[29] H. Ding, X. Bao, Z. Jamili-Shirvan, J. Jin, L. Deng, K. Yao, P. Gong, X. Wang, Enhancing strength-ductility synergy in an ex situ Zr-based metallic glass composite via nanocrystal formation within high-entropy alloy particles, Materials and Design 210 (2021) 110108. doi:10.1016/j.matdes.2021.110108.
URL https://doi.org/10.1016/j.matdes.2021.110108

[30] S. Cardinal, J. M. Pelletier, G. Q. Xie, F. Mercier, Manufacturing of Cu-based metallic glasses matrix composites by spark plasma sintering, Materials Science and Engineering A 711 (2018) 405–414. doi:10.1016/j.msea.2017.11.052.
URL https://doi.org/10.1016/j.msea.2017.11.052

[31] S. Cardinal, J. M. Pelletier, G. Q. Xie, F. Mercier, F. Dalmas, Enhanced compressive plasticity in a Cu-Zr-Al – Based metallic glass composite, Journal of Alloys and Compounds 782 (2019) 59–68. doi:10.1016/j.jallcom.2018.11.300.
URL https://doi.org/10.1016/j.jallcom.2018.11.300

[32] Z. Yang, R. Al-Mukadam, M. Stolpe, M. Markl, J. Deubener, C. Körner, Isothermal crystallization kinetics of an industrial-grade Zr-based bulk metallic glass, Journal of Non-Crystalline Solids 573 (2021). doi:10.1016/j.jnoncrysol.2021.121145.

[33] L. Gautier, S. Cazottes, M. Véron, D. Fabrègue, J. Chevalier, Spherulitic growth process in Ti-based metallic glass: Microstructure, phase identification, and growth mechanism, Materials Characterization 192 (2022) 112170. doi:10.1016/j.matchar.2022.112170.

[34] H. Sun, K. M. Flores, Spherulitic crystallization mechanism of a Zr-based bulk metallic glass during laser processing, Intermetallics 43 (2013) 53–59. doi:https://doi.org/10.1016/j.intermet.2013.06.010.
URL https://www.sciencedirect.com/science/article/pii/S0966979513001830

[35] A. Ericsson, V. Pacheco, J. Marattukalam, R. Dalgliesh, A. Rennie, M. Fisk, M. Sahlberg, Crystallization of a Zr-based metallic glass produced by laser powder bed fusion and suction casting, Journal of Non-Crystalline Solids 571 (2021) 120891. doi:https://doi.org/10.1016/j.jnoncrysol.2021.120891.

URL https://www.sciencedirect.com/science/article/pii/S0022309321002507

[36] M. Newville, R. Otten, A. Nelson, A. Ingargiola, T. Stensitzki, Lmfit: non-linear least-square minimization and curve-fitting for python (2021). doi:https://doi.org/10.5281/zenodo.5570790.

[37] R. M. German, P. Suri, S. J. Park, Review: Liquid phase sintering, Journal of Materials Science 44 (2009) 1–39. doi:10.1007/s10853-008-3008-0.

[38] W. Zhang, J. Huang, X. Yu, G. Liu, H. yanqin, D. Fan, Atomic-level diffusion at the amorphous $Zr_{50}Cu_{50}$/crystalline Cu interface: A molecular dynamics study, Journal of Advanced Joining Processes 6 (2022). doi:10.1016/j.jajp.2022.100120.

[39] J. Eckert, N. Mattern, M. Zinkevitch, M. Seidel, Crystallization behavior and phase formation in ZrAlCuNi metallic glass containg oxygen, Materials Transactions, JIM 39 (1998) 623–632. doi:https://doi.org/10.2320/matertrans1989.39.623.

[40] V. Khonik, N. Kobelev, Metallic glasses: A new approach to the understanding of the defect structure and physical properties, Metals 9 (2019). doi:10.3390/met9050605.

[41] A. V. D. Beukel, J. Sietsma, The glass transition as a free volume related kinetic phenomenon, Acta metall, mater 38 (1990) 383–389.

[42] W. Zhang, Y. Tian, D. C. Liu, F. Wang, B. Yang, B. Q. Xu, Experimental study on the thermal volatilization and condensation of zinc at 10 Pa and 200 Pa, Journal of Materials Research and Technology 9 (2020) 3590–3597. doi:10.1016/j.jmrt.2020.01.097.